IEEE Robotics and Automation Letters (RA-L) paper, presented at ICRA 2026, Vienna, Austria. Cite as RA-L paper.

Distance-Based Shared Control for Vitreoretinal Surgery

Marius Briel, Dongyue Wu, Maximilian Hess, Ludwig Haide, Nicola Piccinelli, *Member, IEEE*, Gernot Kronreif, *Member, IEEE*, Marco Pellegrini, Eleonora Tagliabue, and Franziska Mathis-Ullrich, *Member, IEEE*

***Abstract*—The fragility of ocular tissues combined with the limited surgical workspace demands precise instrument control and focus, making sensor-integrated robotic systems a promising solution. In this letter, we introduce a surgical system for telemanipulated endolaser photocoagulation that leverages instrument-integrated optical coherence tomography (iiOCT) for accurate distance measurement. We have developed a controller that maintains a specified instrument-to-retina distance, complemented by haptic shared control to assist the ophthalmic surgeon throughout the procedure. We conducted a pilot study involving 12 participants, including an expert vitreoretinal surgeon, to evaluate the system's performance across three levels of user assistance. The distance-based controller demonstrated a significant improvement in axial precison compared to telemanipulated trials, achieving a mean error of 4 μm and a standard deviation of 69 μm across all subjects. Experiments conducted on porcine eyes confirmed the feasibility of our approach on ex vivo tissues.**

***Index Terms*—Medical robots and systems, sensor-based control, human factors and human-in-the-loop.**

I. Introduction

VITREORETINAL surgery encompasses a range of micron-scale procedures aimed at restoring, preserving, and enhancing vision for various retinal conditions. It involves procedures conducted within the eye's interior using instruments such as cannulas, forceps, or endolaser probes, where precision is key. The success and safety of these procedures are critically dependent on the surgeon's depth perception, hand-eye coordination, and dexterity. Surgeons primarily rely on the size of shadows cast by instruments to estimate micrometer-scale distances and shapes, while contending with tremors that measure around 100 μm [1].

Endolaser photocoagulation is a common treatment for various retinal diseases, utilizing laser energy delivered by a fiber-integrated endoprobe positioned close to the retina. In panretinal photocoagulation, up to 2000 laser spots may be applied over a treatment duration of up to 30 minutes, making this procedure both tedious and physically demanding for the surgeon [2]. Maintaining a consistent instrument-to-retina distance throughout an extended session is challenging but critical for controlling the size and energy density of each laser spot [3]. Excessive energy deposition and absorption can lead to irreversible retinal damage, while insufficient energy delivery may fail to achieve the desired therapeutic effect.

To address the challenges in vitreoretinal surgery, various robotic systems integrated with optical sensors have been proposed [4]. These systems offer numerous advantages, including motion scaling, tremor reduction and distance detection. There is ongoing debate regarding the optimal presentation of distance information; while visual cues can be distracting, auditory signals may go unnoticed [5]. Conversely, across multiple fields of robot-assisted surgery, haptic feedback has consistently demonstrated a strong positive impact on accuracy, success rates, and completion times in numerous studies [6].

The main contributions of this work are as follows:

1) Design of a distance-based shared control system: We propose a shared control system for endolaser photocoagulation, integrating a robotic manipulator as the actuator, an input device for transmitting user movements and providing haptic feedback, an optical coherence tomography (OCT) engine, a surgical laser source, and an endolaser OCT instrument as the end-effector. The shared control system (see Fig. 1) features a distance-based robotic control algorithm that maintains a constant distance from the retina and provides distance-based haptic feedback to the surgeon via the input device, aiming to reduce the physical and mental workload during the procedure.

2) Integration of an instrument-integrated optical coherence tomography (iiOCT) distance sensor: iiOCT has emerged as a promising sensory technology, offering high-resolution intraocular measurements of instrument-to-tissue distances that surpass those provided by surgical microscopy or microscope-integrated

Received 24 July 2025; accepted 8 November 2025. Date of publication 8 December 2025; date of current version 24 December 2025. This article was recommended for publication by Associate Editor H. Kajimoto and Editor K.-U. Kyung upon evaluation of the reviewers' comments. *(Corresponding author: Marius Briel.)*

Marius Briel is with the Carl Zeiss AG, 73447 Oberkochen, Germany, and also with the Laboratory for Surgical Planning and Robotic Cognition (SPARC), Friedrich-Alexander-University, 91054 Erlangen-Nürnberg, Germany (e-mail: marius.briel@zeiss.com).

Dongyue Wu is with the Carl Zeiss AG, 73447 Oberkochen, Germany, and also with the Department of Microsystems Engineering, University of Freiburg, 79098 Freiburg im Breisgau, Germany.

Maximilian Hess, Ludwig Haide, and Eleonora Tagliabue are with the Carl Zeiss AG, 73447 Oberkochen, Germany.

Nicola Piccinelli is with the Department of Engineering for Innovation Medicine, University of Verona, 37129 Verona, Italy.

Gernot Kronreif is with the Austrian Center of Medical Innovation and Technology (ACMIT), 2700 Wiener Neustadt, Austria.

Marco Pellegrini is with the Department of Translational Medicine, University of Ferrara, 44121 Ferrara, Italy.

Franziska Mathis-Ullrich is with the Laboratory for Surgical Planning and Robotic Cognition (SPARC), Friedrich-Alexander-University, Erlangen-Nürnberg, 91054 Erlangen, Germany.

Digital Object Identifier 10.1109/LRA.2025.3641113

IEEE Robotics and Automation Letters (RA-L) paper, presented at ICRA 2026, Vienna, Austria. Cite as RA-L paper.

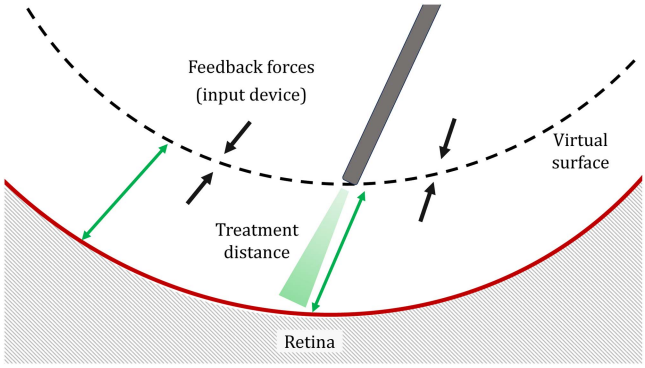

Fig. 1. In our shared control mode, the robotically held instrument maintains a constant axial distance from the retina by navigating along a virtual surface. Concurrently, haptic feedback forces guide the surgeon towards this virtual surface within the input device coordinate system.

OCT. To integrate this sensor, we developed a surgical instrument that combines both the surgical laser fiber and the OCT sensing fiber.

3) Evaluation by a surgeon and ex vivo testing: We conduct a pilot study with non-expert users and an expert vitreoretinal surgeon to demonstrate the advantages of our distance-based shared control system using a phantom eye model. Additionally, we validate its applicability with ex vivo porcine eyes.

II. Related Work

Robotic systems in ophthalmic surgery encompass both handheld and telemanipulated systems [7]. Notable examples of these systems are Micron [8], Steady-Hand [9], and the RAMIS ophthalmic micromanipulator [10]. While these robotic systems facilitate precise instrument positioning, the integration of sensors is essential for active assistance.

Balicki et al. were the first to integrate fiber-based OCT into a surgical pick held by a Cartesian positioning robot, enabling the maintenance of a constant distance from a vertically oscillating flat surface [11]. While they achieve precise surface tracking, their artificial phantom is flat, and the probe is positioned perpendicular to the surface for optimal signal. Lee et al. introduced an OCT-based tool-to-retina distance control method using a handheld microsurgical tool [12]. They employed a U-Net architecture to estimate the retinal boundary position and controlled the axial motor to compensate for unwanted axial movements. This method is designed for subretinal injection to eliminate micron-scale tremor, whereas depth perception and positioning are more critical in extensive photocoagulation surgery. Yu et al. proposed a dual-rate controller that employs low-frequency OCT feedback alongside high-frequency position servoing [13]. However, the high computational cost of B-scan dewarping and the slow OCT feedback rate of $5\,\mathrm{Hz}$ limited accurate tracking to low speeds below $0.5\,\mathrm{mm/s}$.

In a vitreoretinal simulation environment, haptic feedback has demonstrated its effectiveness in reducing surgical durations and minimizing the risk of accidental damage [14]. Mieling et al. proposed utilizing axial OCT measurements instead of force measurements to provide distance-based haptic force feedback during needle insertion in a non-ophthalmic context. This approach offers feedback before contact occurs [15]. Additionally, Barthel et al. developed a telemanipulation framework for vitreoretinal surgery that employs their hybrid parallel-serial micromanipulator in conjunction with a Phantom Premium input device [16]. In this framework, haptic feedback is generated based on the difference between the input device and remote side positions, with plans to incorporate force sensors for enhanced feedback.

Yang et al. investigated the use of their handheld Micron robot for automated laser photocoagulation, employing high-resolution optical motion tracking to determine the pose of the instrument tip [17]. Visual servoing controls the planar movement, while the axial movement is controlled to maintain a constant distance from the retinal surface [18], [19]. However, Micron's limited motion range of $4\,\mathrm{mm}$ confines its application to specific target areas with few laser spots, such as retinal tear treatments. Additionally, the method is impeded by challenges in camera calibration, 3D reconstruction, and zoom optics. An automated panretinal photocoagulation system is presented in [20], featuring a magnetically steered endolaser probe guided by camera feedback. Experiments are performed on a spherical phantom eye, but both equidistant treatment pattern planning and evaluation rely on 2D images from a monoscopic camera, neglecting retinal surface topology. The eye's optics and wide-angle retinal viewing systems introduce complex distortions that are difficult to simulate [21], even with biometric data, advocating for intraocular iiOCT, which is unaffected by these distortions. Consequently, their method is unsuitable for closed-sky ex vivo porcine eye experiments, a vital step toward clinical application.

In summary, although fiber-based iiOCT for distance detection and control is well-established, it has not been applied in telemanipulated systems or specifically for endolaser photocoagulation. Moreover, distance-based haptic shared control introduces a novel approach in vitreoretinal surgery.

III. Methods

The algorithmic components include the control unit and the haptic unit, both of which rely on distance information provided by the OCT processing unit. The shared control component integrates user inputs with distance measurements to effectively control the robotic manipulator (Fig. 2).

A. OCT Processing

During surgery, once the instrument is inserted into the intraocular space, the iiOCT captures interference patterns that require preprocessing and processing to extract distance measurements. The OCT preprocessing steps include the reconstruction of raw interferometer data, averaging, background subtraction, and the application of a $10\,\mathrm{mm}$ window in the spatial domain. To extract distances from the preprocessed OCT data, a peak search algorithm detects two signal peaks: the first corresponds to the probe tip, and the second to the target object. The initial back-reflection occurs at the interface between the optical fiber tip and the environment, forming the first signal peak. The

IEEE Robotics and Automation Letters (RA-L) paper, presented at ICRA 2026, Vienna, Austria. Cite as RA-L paper.

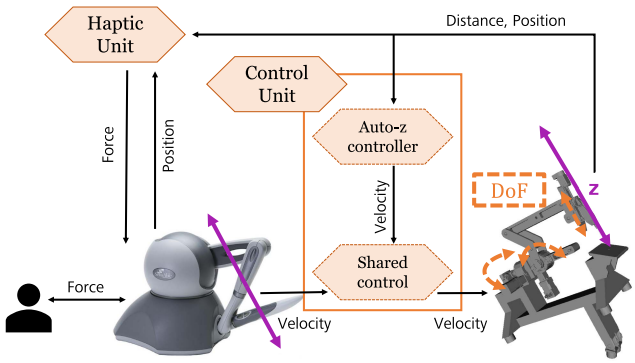

Fig. 2. The key algorithmic components of the system comprise the control unit and the haptic unit, both of which rely on OCT distance information and robot positions. The shared control system integrates user inputs with distance commands.

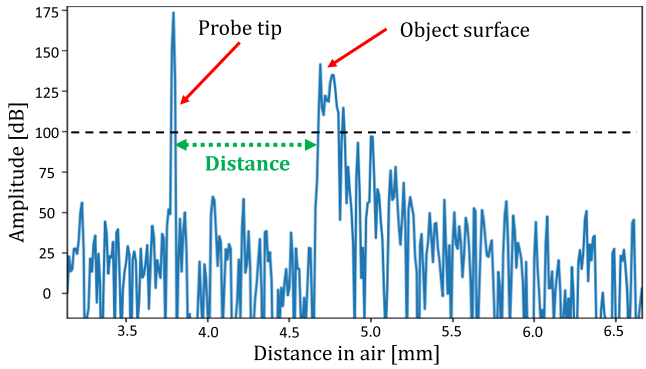

Fig. 3. Peak search to extract distance data from OCT A-scans, with a minimum peak height threshold set at 100 dB.

distance between these peak locations provides the distance from the fiber tip to the retina (Fig. 3).

B. Haptic Shared Control With Auto-Z Depth Regulation

The shared control unit in Fig. 2 issues target joint velocities for all three degrees of freedom (DoFs) of the robotic manipulator. The proposed *Auto-z controller* autonomously regulates the axial distance between the instrument tip and the retina, referred to as the *controlled variable*. Specifically, it controls the insertion depth z of the instrument by adjusting the velocity of the third joint, the designated *control element*. In this shared control scheme, user commands for the third joint are ignored, as this joint is governed by the Auto-z controller. The user is responsible for selecting the laser delivery location on the retina (lateral motion), while the insertion depth is autonomously managed, as depth perception is typically challenging in retinal surgery.

The user interacting with the haptic device produces a Cartesian velocity vector $\boldsymbol{v}_o$ which, upon homogeneous transformation $\boldsymbol{T}_o^r$, defines the desired linear velocity command for the remote instrument tip

$$\boldsymbol{v}^d = \boldsymbol{T}_o^r \boldsymbol{v}_o \in \mathbb{R}^3, \tag{1}$$

expressed in the base frame of the remote robot. Due to the presence of a mechanical remote center of motion (RCM) constraint, the 3-DoF manipulator only allows translational movements; rotational components are excluded.

Given the current joint configuration $\boldsymbol{q} \in \mathbb{R}^3$, the system's differential forward kinematics are described by the Jacobian $\boldsymbol{J}(\boldsymbol{q}) \in \mathbb{R}^{3\times3}$, which maps joint velocities to Cartesian velocities under the RCM constraint. The desired joint velocities $\dot{\boldsymbol{q}}^d \in \mathbb{R}^3$ are computed as

$$\dot{\boldsymbol{q}}^d = \boldsymbol{J}(\boldsymbol{q})^{-1} \boldsymbol{v}^d. \tag{2}$$

To regulate the insertion depth, the velocity of the third joint is overridden by the output of the Auto-z controller, implemented as a proportional-derivative (PD) controller that uses real-time axial distance measurements from an OCT system. Let $y(t)$ represent the current distance between the instrument tip and the retina, and let r be the desired target distance. The commanded velocity for the third joint is given by

$$\dot{q}_3^z = -k_p(br - y(t)) - k_d \frac{cr - y(t)}{T_f + \dot{y}(t)}, \tag{3}$$

where k_p and k_d are the control gains, T_f is a filter constant, and $b, c \in \mathbb{R}$ are shaping parameters. The distance derivative is approximated in discrete time as

$$\dot{y}(t) \approx \frac{y(t) - y(t - T_s)}{T_s}, \tag{4}$$

with sampling period T_s. The final joint velocity command $\dot{\boldsymbol{q}}^r$ sent to the robot's low-level controller is

$$\dot{\boldsymbol{q}}^r = \begin{bmatrix} \dot{q}_1^d \\ \dot{q}_2^d \\ \dot{q}_3^z \end{bmatrix}, \tag{5}$$

where $\dot{q}_1^d$ and $\dot{q}_2^d$ are from (2), and $\dot{q}_3^z$ is determined by the depth controller in (3).

Depth feedback is provided to the operator by rendering a unidirectional haptic force along the instrument's insertion axis. A virtual joint torque for the third joint is defined as

$$\tau_3^h = k_F(r - y(t)), \tag{6}$$

where k_F is the haptic feedback gain. From this, the complete virtual joint torque vector becomes

$$\boldsymbol{\tau}^h = \begin{bmatrix} 0 \\ 0 \\ \tau_3^h \end{bmatrix}. \tag{7}$$

The joint torque is then mapped to Cartesian space via

$$\boldsymbol{f}^h = \boldsymbol{J}(\boldsymbol{q})^{-\top} \boldsymbol{\tau}^h, \tag{8}$$

yielding the Cartesian force vector $\boldsymbol{f}^h \in \mathbb{R}^3$, aligned with the instrument axis. This force is transformed to the haptic device's reference frame via $\boldsymbol{T}_r^o = (\boldsymbol{T}_o^r)^{-1}$ and rendered to the user as depth guidance

$$\boldsymbol{f}_o = \boldsymbol{T}_r^o \boldsymbol{f}^h. \tag{9}$$

Haptic feedback provided solely in the instrument axis aims to improve targeting accuracy and alleviate the cognitive burden of depth estimation. To assist the surgeon in achieving the ideal

IEEE Robotics and Automation Letters (RA-L) paper, presented at ICRA 2026, Vienna, Austria. Cite as RA-L paper.

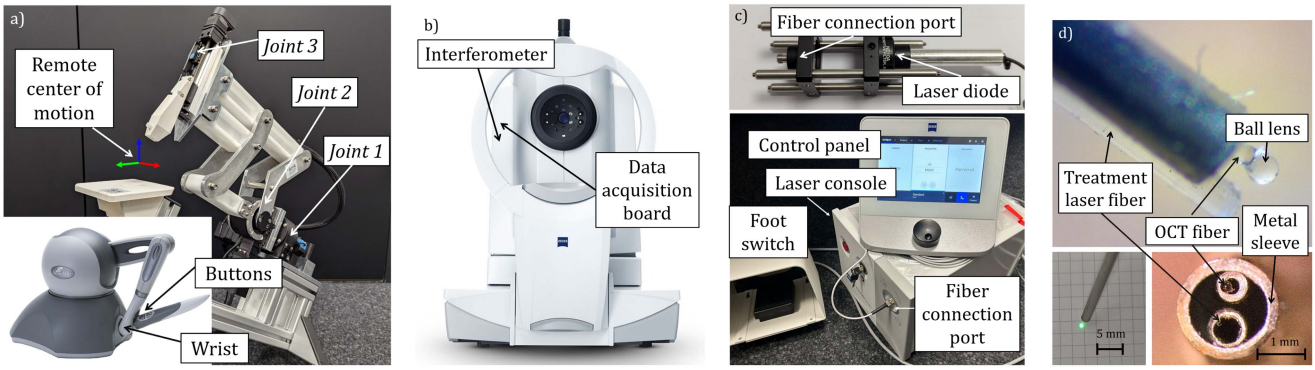

(a) Robot and input device (b) OCT engine (c) Laser sources (d) Instrument

Fig. 4. System overview: (a) Robotic manipulator with indicated RCM and joints, along with the Phantom Omni input device, (b) IOL Master 700 in the configuration utilized for this study, as well as its original configuration, (c) Laser diode used for the pilot study and VISULAS green surgical laser employed in the porcine eye experiments, (d) Magnified images of the combined fiber tips and the laser spot of the manufactured instrument.

working distance for laser delivery, the haptic feedback directs the user toward a virtual surface offset from the retinal geometry (Fig. 1). This ensures intuitive guidance for depth positioning without interfering with lateral control.

C. Auto-Z Controller Parameters Identification

Model identification was performed using MATLAB System Identification. A linear model was employed to approximate the system dynamics by analyzing the responses to an input test signal, achieving a correlation of $87.43\,\%$. The transfer function is specified as discrete, with a sampling time of $T_s = 0.02\,\mathrm{s}$. Direct modeling was not feasible due to the intermediary programmable logic controller (PLC) controlling the motor for joint 3, as well as the dead times introduced by Robot Operating System (ROS) integration.

MATLAB PID Tuner was utilized to select a controller structure and obtain an initial parametrization $k_p = 0.04688$, $k_d = 0.01809$, $T_f = 0.02231$. Given the controller described in (3), the transfer function could not fully capture the real system dynamics, as reflected by the correlation value. Consequently, the baseline parameters obtained from PID Tuner required refinement on the actual setup. The fine-tuned controller parameters are $k_p = 0.02791$, $k_d = 0.01552$, $T_f = 0.01468$, with $a = b = 1$. The system exhibits a rise time of $1.72\,\mathrm{s}$ and a settling time of $1.99\,\mathrm{s}$, which are suboptimal for real-time applications. Attempts to accelerate the step response led to instabilities within the closed-loop system.

For the force feedback, a relatively low feedback gain of $k_F = 5000$ was chosen in response to intermittent irregularities observed, which were attributed to erroneous OCT data.

IV. Experimental Setup

The robotic manipulator [22], a three-degree-of-freedom manipulator depicted in Fig. 4(a), features a parallel kinematic structure that provides a mechanical RCM. With the RCM as a movement constraint, the pivoting range is $\pm 40^\circ$ for both rotating axes (*joint 1* and *joint 2*) around the RCM and the linear instrument insertion range (*joint 3*) is $100\,\mathrm{mm}$. The robot can be directly connected to a computer via TCP-IP and supports both position-based and velocity-based control with an update frequency of $50\,\mathrm{Hz}$.

The Phantom Omni (*SensAble Inc., Massachusetts, US*), depicted in Fig. 4(a), serves as the input device, allowing users to specify the desired position of the robot's end-effector while receiving haptic feedback up to $3.3\,\mathrm{N}$ at a fixed update frequency of $50\,\mathrm{Hz}$. In our work, wrist Cartesian velocities govern the end-effector velocity, while two buttons are configured for laser activation and clutching.

The swept-source OCT engine ZEISS IOL Master 700 (*Carl Zeiss Meditec AG, Jena, Germany*), depicted in Fig. 4(b), is utilized in this work. It operates at a central wavelength of $1060\,\mathrm{nm}$, with an imaging depth (in air) of approximately $60\,\mathrm{mm}$ and an axial resolution of approximately $30\,\mu\mathrm{m}$, along with an A-scan rate of $30\,\mathrm{kHz}$. The accuracy of distance sensing was validated by comparing measured step sizes to robotic motion step sizes of $300\,\mu\mathrm{m}$, excluding outliers with deviations exceeding $200\,\mu\mathrm{m}$ from the mean. On an open sky porcine eye, the mean error was $3.1\,\mu\mathrm{m}$ with a standard deviation of $18.2\,\mu\mathrm{m}$. To acquire real-time OCT signals for feedback control, we directly access the data acquisition board to stream the interferometer readouts over USB 3.0 to an external PC, where the A-scan reconstruction and processing are performed. The data is streamed at $120\,\mathrm{Hz}$.

The ZEISS VISULAS green (*Carl Zeiss Meditec AG, Jena, Germany*), depicted in Fig. 4(c), is used for laser photocoagulation, featuring a wavelength of $532\,\mathrm{nm}$ and a maximum power output of $1.5\,\mathrm{W}$, along with a low-power aiming beam at $650\,\mathrm{nm}$. For experiments not involving animal models, a low-power $532\,\mathrm{nm}$ laser diode (CPS532-C2, *Thorlabs GmbH, Bergkirchen, Germany*) is utilized, whereas the surgical laser source is employed in ex vivo porcine eye experiments.

For this study, we developed a surgical instrument that integrates a surgical laser fiber with a sensing fiber. The OCT probe used in this work consists of a ball-lensed single-mode optical fiber protected by a metal ferrule (*LaseOptics*), achieving a working distance of $2\,\mathrm{mm}$ in water. For surgical laser delivery, a multi-mode optical fiber (M14L02, *Thorlabs*) with a numerical aperture (NA) of 0.22 is utilized. The multi-mode fiber is stripped

IEEE Robotics and Automation Letters (RA-L) paper, presented at ICRA 2026, Vienna, Austria. Cite as RA-L paper.

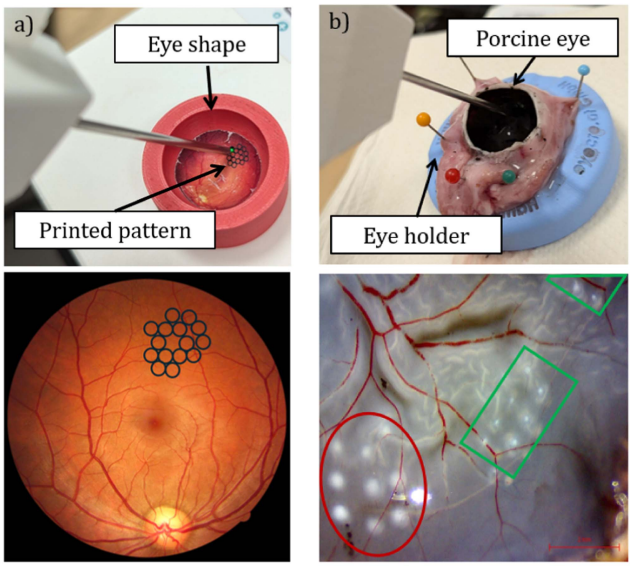

(a) Printed eye shape (b) Porcine eye

Fig. 5. Test objects used: (a) Eye model with a treatment pattern designed for retinal tears, (b) Porcine eye with lesions marked in red without assistance and marked in green with the assistance of the Auto-z controller.

and cleaved, then inserted into a 700 µm diameter metal sleeve. To facilitate simultaneous operation of OCT sensing and laser delivery, both sleeves are glued together and encased within a 2 mm diameter protective sleeve, as shown in Fig. 4(d). The top image displays the dual-fiber instrument without the multi-mode fiber sleeve and dual-fiber protective sleeve for clearer visualization.

V. Experimental Validation

To evaluate our distance-based shared control system, we conducted a pilot study with non-expert users, followed by testing with an expert vitreoretinal surgeon. Additionally, we demonstrate the applicability of our system to ex vivo porcine eyes. Participants are tasked with treating a simulated retinal tear by applying laser shots to 15 designated locations on the retina, as illustrated in Fig. 5(a). A 3D-printed spherical eye model with a radius of 10 mm, featuring a printed treatment pattern, is used as the target. Multiple ring patterns are commonly arranged for retinal tears [23]. A hands-free table magnifier is provided to enhance visibility of the surgical scene. The objective is to deliver laser treatment to the center of each target circle while maintaining a constant distance of 3 mm from the retina, particularly during the activation of the laser. Prior to the study, participants are given 10 min to familiarize themselves with the system. Each participant then completes three trials, each with a different type of assistance:

- *Mode 1:* The user has full control over the movements of the instrument tip, with the input device freely movable in all directions.
- *Mode 2:* The Auto-z controller is activated to manage the distance to the retina. The user no longer controls the z position of the instrument tip but retains control over its lateral positioning. No haptic feedback.
- *Mode 3:* In addition to the Auto-z controller from Mode 2, haptic feedback is now provided along the instrument axis via the input device.

The order of the assistance modes is randomized to prevent any learning effects from influencing the study results. The eleven non-expert participants have no prior experience with vitreoretinal surgery or surgical robotic systems. In contrast, the retinal surgeon has five years of surgical experience and limited familiarity with the robotic system.

To evaluate the accuracy and precision of distance control, the distance from the instrument tip to the retinal surface is continuously measured from the first laser trigger to the last. Additionally, they are assessed separately at the specific time points of laser delivery. Accuracy refers to how close measurements are to the target distance (*mean error*), indicating how well users can judge the correct depth level on average. Precision describes the consistency of a user's measurements (*standard deviation (SD)*), reflecting the ability to maintain a constant distance. To assess cognitive workload, participants are asked to complete the NASA Task Load Index (TLX) questionnaire for each mode. This involves rating the workload across six dimensions: mental demand, physical demand, temporal demand, performance, effort, and frustration.

The porcine eye experiment is conducted under 'open sky' conditions, meaning the cornea, lens, and vitreous are removed (Fig. 5(b)), to minimize unwanted retinal detachment during instrument maneuvering. The evaluation of the Auto-z controller is based on the uniformity of visually discernible lesions, the standard in retinal endolaser photocoagulation, offering a qualitative comparison with unassisted surgery [24]. Additionally, the iiOCT data is used to analyze the performance of the controller.

VI. Results

A. Distance Control Accuracy

Figure 6 illustrates Subject 1's distance control performance across various modes, highlighting the enhanced effectiveness of automated Modes 2 and 3 compared to the unassisted Mode 1. Vertical lines indicate the frequency of laser activation, and red dots denote the distance value at each instance of laser triggering. The horizontal lines indicate the target distance of 3 mm with an permissible deviation of ±500 µm to ensure lesion uniformity. In Mode 1, the tolerance is exceeded for nine out of fifteen laser triggers (red dots), resulting in an error rate of 60 %. Conversely, in Modes 2 and 3, the error rate for laser delivery is 0 %.

Table I presents the distance control performance of Subject 1 and the retinal surgeon across different modes. A paired t-test confirms significant error reduction ($p < 0.0001$) for Subject 1's laser spots in Modes 2 and 3, achieving over 95.4 % reduction in distance error and 74.7 % reduction in SD. The mean error difference between Mode 1 and Mode 2 is 0.70 mm, with a 95 % confidence interval from 0.43 mm to 0.98 mm. Statistical significance is greater overall due to a larger sample size. The surgeon outperforms study participants in Mode 1 and achieves comparable results in Modes 2 and 3, reducing completion time

IEEE Robotics and Automation Letters (RA-L) paper, presented at ICRA 2026, Vienna, Austria. Cite as RA-L paper.

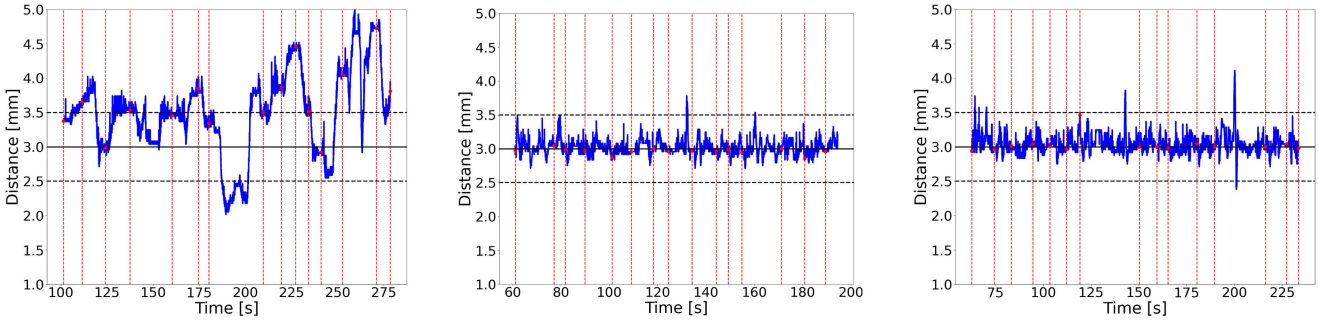

(a) Mode 1 (b) Mode 2 (c) Mode 3

Fig. 6. Instrument-to retina distance measurements over time for subject 1. The red vertical lines mark the time point of laser triggering. The tolerance levels for the instrument-to-retina distances are indicated by black dashed lines. Subject 1 is selected as a representative example, reflecting typical participant results, due to incomplete data for the retinal surgeon.

TABLE I
MEAN AND STANDARD DEVIATION OF INSTRUMENT-TO-RETINA DISTANCE MEASUREMENTS DURING THE ENTIRE TRIAL (*OVERALL*) AND FOR THE TIME POINTS OF LASER DELIVERY (*LASER*). DURATION IS DEFINED AS THE TIME SPAN FROM THE INITIAL TO THE FINAL LASER TRIGGER.

User	Mode	Mean [mm]		SD [mm]		Duration
		Overall	Laser	Overall	Laser	[s]
Subject 1	1	3.499	3.671	0.571	0.487	177
	2	3.016	**2.970**	**0.114**	**0.050**	**133**
	3	**3.011**	3.031	0.139	0.123	171
Retinal surgeon	1	2.976	-	1.293	-	46
	2	**3.006**	3.044	**0.110**	0.102	37
	3	3.019	-	0.125	-	**25**

User	Mode	Error reduction		SD reduction		Time
		Overall	Laser	Overall	Laser	saving
Subject 1	1→2	96.8 %	95.5 %	80.0 %	89.7 %	44 s
	1→3	97.8 %	95.4 %	75.7 %	74.7 %	6 s
Retinal surgeon	1→2	75.0 %	-	91.5 %	-	9 s
	1→3	20.8 %	-	90.3 %	-	21 s

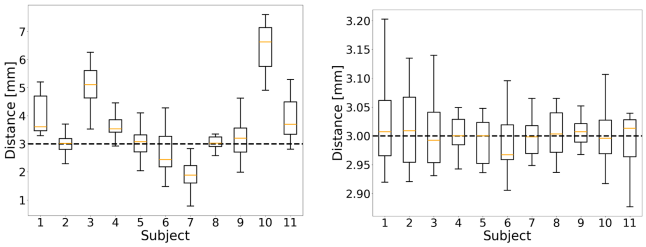

(a) Mode 1 (b) Mode 3

Fig. 7. Boxplot of distances at laser treatment times, with the optimal distance of 3 mm marked by a black dashed line.

to 25 s compared to 96 s for non-experts. Laser triggers were recorded only in Mode 2, as the clutch button was pressed instead of the laser activation button.

Fig. 7 displays the boxplot of the distances at laser treatment times for each subject without (Mode 1) and with (Mode 3) assistance. In Mode 1, intra- and inter-subject variability is large, as participants struggle to accurately identify or maintain the 3 mm distance. The mean laser delivery distance across all subjects is 3.010 mm for Mode 2 and 3.004 mm for Mode 3, showing minimal user dependence. In Modes 2 and 3, all participants consistently remain within the specified tolerance limits, while Mode 1 has an error rate of 58.2 %.

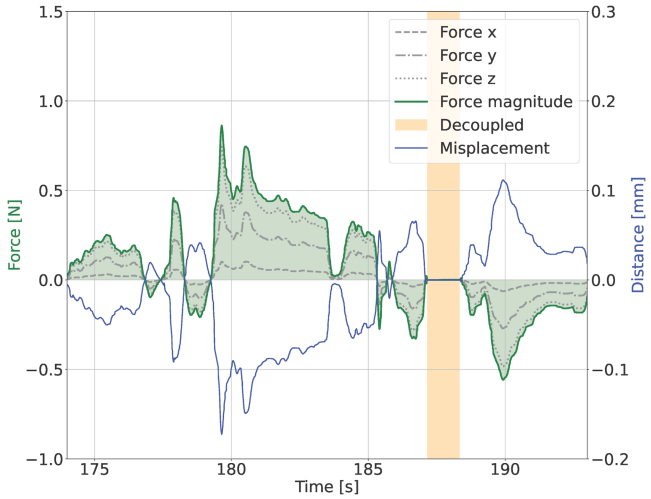

Fig. 8. Haptic feedback force in the trial of subject 1 that is generated in response to mismatched tool-to-retina distance from the ideal value in Auto-z mode.

B. Workload Assessment

Fig. 8 displays the force magnitude generated by the haptic unit at the input device during Mode 3. The force components F_x, F_y, and F_z within the input device coordinate system contribute to the total force F, which is directly proportional to the deviation of the current user input from the ideal position that the user is guided towards. The ideal position refers to the location that the remote side is controlled to, specifically, the position that is 3 mm away from the retina. The yellow bar indicates the decoupling of the input device from the remote side by pressing a button, which is essential when the limits are reached.

Fig. 9 presents the NASA TLX scores for all participants across the different modes, measured on a scale from 0 (very low) to 19 (very high). Modes 2 and 3 perform similarly, with scores ranging from 3.3 for physical demand to 6.6 for effort. In contrast, the Mode 1's workload is rated between 7.9 for temporal demand to 12.7 for effort. The effect of distance control (Mode 2) and haptic feedback (Mode 3) on workload compared to baseline Mode 1 is significant ($p < 0.002$) for all dimensions except temporal ($p = 0.09$, $p = 0.12$) and physical ($p = 0.015$).

IEEE Robotics and Automation Letters (RA-L) paper, presented at ICRA 2026, Vienna, Austria. Cite as RA-L paper.

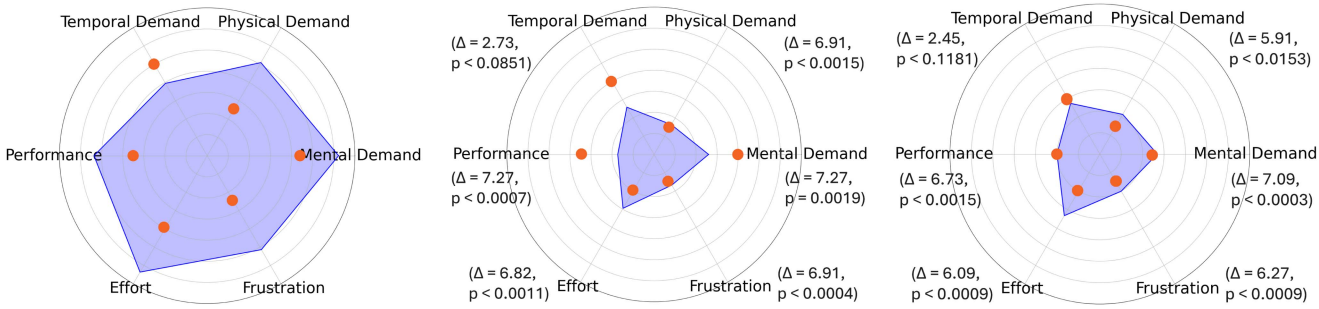

(a) Mode 1 (b) Mode 2 (c) Mode 3

Fig. 9. Results of the NASA TLX assessment across all subjects (blue hexagon) and the surgeon (orange dot). The distance from the center along the six dimensions corresponds to the workload, measured from 0 (very low) to 19 (very high).

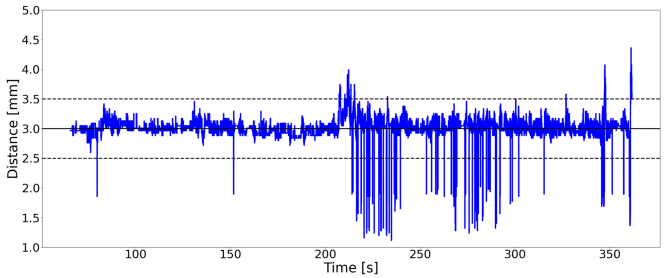

Fig. 10. Distance measurements during the porcine eye experiment by a non-expert using the Auto-z controller.

Mean NASA TLX ratings improve by 2.5 to 7.3 (Δ in Fig. 9) across dimensions. The feedback was deemed intuitive and beneficial by the surgeon, as evidenced by the low frustration and mental demand scores (orange dots). Despite occasionally perceiving it as bouncy, the ability to discern surface geometry through haptic feedback was valued. With automatic control of the distance, the surgeon was able to focus exclusively on lateral instrument placement, which helped alleviate workload and shorten the procedure duration.

C. Porcine Eye Experiment

Fig. 5(b) presents the lesions induced by endolaser using different control modes. Generally, the spots set with Auto-z exhibit more uniform diameters compared to those controlled manually. Fig. 10 displays the measured distance data (mean: $3.01\,\mathrm{mm}$, SD: $0.189\,\mathrm{mm}$) throughout the experiment, revealing that the distance between the retina and the instrument tip frequently exceeds the tolerance limits after $200\,\mathrm{s}$.

VII. Discussion

Our distance-based shared control system, which incorporates the Auto-z controller and haptic feedback, achieves a mean error of only $4\,\mu\mathrm{m}$ from the target distance, with a SD of $69\,\mu\mathrm{m}$, which is below the average tremor of surgeons [1]. This demonstrates the controller's superiority over manual surgery in maintaining a consistent distance. Due to the robot's latency, the controller is designed to operate at a slower pace to ensure stability, which results in larger distance errors during rapid movements. Moreover, inaccurate distance measurements can lead to incorrect responses from the controller. However, further down-sampling of measurements would reduce the controller's update rate, impacting the closed-loop system. In contrast to other photocoagulation systems [17], [20], where the laser delivery position is automatically controlled, we propose to allow surgeons to manage lateral positioning while automating only the safety-critical distance control. This approach allows surgeons to select areas to treat and avoid in real-time. In future work, we may also consider extending automation to lateral positioning.

The mental workload perceived by participants decreased by $56.3\,\%$ when assisted by the controller. The strong consistency between the input device and the instrument tip when haptic feedback is enabled illustrates its effectiveness in guiding the surgeon toward the virtual surface. Participants who were not fond of the haptic feedback struggled to interpret the forces. Overall, human-machine interaction improved when participants could understand the haptic feedback. Furthermore, other feedback methods, such as visual feedback, could augment the shared control experience. With the distance automatically maintained, participants complete the surgeries more quickly. However, in comparison to other systems [17], [20], the surgeon's average time of $1.7\,\mathrm{s}$ per laser point is relatively slow. It is important to note that these systems are fully automated, whereas our shared control system is not primarily designed for rapid operation. For our system, achieving faster robot movements necessitates reducing the settling time of our controller, which in turn requires a faster reaction time from the robot, making adjustments to the robot's inner controller necessary. The time per laser point is likely to decrease as users become more familiar with the system. Participants in the user study showed improvement over time, regardless of the different modes, with few exceptions. In consecutive trials of the same subject, the total duration decreased in 16 out of 22 transitions, with an average reduction of $18\,\%$, indicating a learning effect.

The effect of inaccurate OCT measurements on the Auto-z controller is noticeable in the porcine eye experiment. The increase in outliers after $200\,\mathrm{s}$ is attributed to evaporated fluid on the retinal surface produced during coagulation, which adheres to the tip of the OCT fiber and disrupts distance measurements. Moreover, even without these impairments, OCT

distance measurements show more fluctuations in porcine eyes due to the lower signal strength from bio-tissue compared to a paper target. The signal is expected to be stronger in water, as the reflection at the lens-water interface would be reduced. To enhance the reliability of the OCT signals, improved segmentation algorithms, such as those based on deep learning, could bolster the robustness of distance detection [12]. Additionally, algorithms designed to detect [25] and potentially correct erroneous signals could be utilized, for instance, by employing intraoperative geometric models to supplement the sensor [26], [27]. Nonetheless, the experiment illustrates the effectiveness of the Auto-z controller in a more realistic setting, as evidenced by the consistent size of the lesions. Refined instrument designs could help reduce the lateral offset between the optical path and the surgical laser, thereby enhancing accuracy. A significant step toward clinical adoption involves the use of curved or flexible instruments [28] to facilitate treatment of peripheral areas that are inaccessible with straight instruments.

VIII. Conclusion

The proposed Auto-z controller effectively maintained a constant distance between the instrument tip and the retina using precise OCT distance values; however, it faced challenges due to unreliable measurements from ex vivo tissue. The haptic feedback mechanism alleviated workload and minimized discrepancies between the input device and the robotic manipulator. Future work will focus on increasing control speed by integrating new motors, with particular emphasis on the joint responsible for depth insertion. In summary, this shared control system holds significant promise for enhancing the effectiveness and safety of photocoagulation procedures and various vitreoretinal surgeries.

References

[1] C. N. Riviere, R. S. Rader, and P. K. Khosla, "Characteristics of hand motion of eye surgeons," in *Proc. IEEE 19th Annu. Int. Conf. Eng. Med. Biol. Soc.*, 1997, pp. 1690–1693.

[2] F. Kuhn, *Vitreoretinal Surgery: Strategies and Tactics*. Cham: Springer, 2016.

[3] R. W. Acheson, M. Capon, R. J. Cooling, P. K. Leaver, J. Marshall, and D. McLeod, "Intraocular argon laser photocoagulation," *Eye*, vol. 1, pp. 97–105, 1987.

[4] E. Vander Poorten et al., "36 - robotic retinal surgery," in *Proc. Handbook Robotic Image-Guided Surg.*, 2020, pp. 627–672.

[5] J. A. Griffin, W. Zhu, and C. S. Nam, "The role of haptic feedback in robotic-assisted retinal microsurgery systems: A systematic review," *IEEE Trans. Haptics*, vol. 10, no. 1, pp. 94–105, Jan.–Mar. 2017.

[6] M. Bergholz, M. Ferle, and B. M. Weber, "The benefits of haptic feedback in robot assisted surgery and their moderators: A meta-analysis," *Sci. Rep.*, vol. 13, no. 1, 2023, Art. no. 19215.

[7] E. Z. Ahronovich, N. Simaan, and K. Joos, "A review of robotic and OCT-aided systems for vitreoretinal surgery," *Adv. Ther.*, vol. 38, pp. 2114–2129, 2021.

[8] R. A. MacLachlan, B. C. Becker, J. C. Tabarés, G. W. Podnar, L. A. Lobes, and C. N. Riviere, "Micron: An actively stabilized handheld tool for microsurgery," *IEEE Trans. Robot.*, vol. 28, no. 1, pp. 195–212, Feb. 2012.

[9] B. Mitchell et al., "Development and application of a new steady-hand manipulator for retinal surgery," in *Proc. IEEE Int. Conf. Robot. Automat.*, 2007, pp. 623–629.

[10] M. A. Nasseri et al., "The introduction of a new robot for assistance in ophthalmic surgery," in *Proc. IEEE 35th Annu. Int. Conf. Eng. Med. Biol. Soc.*, 2013, pp. 5682–5685.

[11] M. Balicki et al., "Single fiber optical coherence tomography microsurgical instruments for computer and robot-assisted retinal surgery," in *Proc. Med. Image Comput. Comput.-Assisted Interv.*, 2009, pp. 108–115.

[12] S. Lee and J. Kang, "CNN-based CP-OCT sensor integrated with a subretinal injector for retinal boundary tracking and injection guidance," *J. Biomed. Opt.*, vol. 26, no. 6, 2021, Art. no. 068001.

[13] H. Yu, J.-H. Shen, K. M. Joos, and N. Simaan, "Calibration and integration of b-mode optical coherence tomography for assistive control in robotic microsurgery," *IEEE/ASME Trans. Mechatron.*, vol. 21, no. 6, pp. 2613–2623, Dec. 2016.

[14] A. Francone, J. M. Huang, J. Ma, T.-C. Tsao, J. Rosen, and J.-P. Hubschman, "The effect of haptic feedback on efficiency and safety during preretinal membrane peeling simulation," *Transl. Vis. Sci. Technol.*, vol. 8, no. 4, 2019, Art. no. 2.

[15] R. Mieling et al., "Proximity-based haptic feedback for collaborative robotic needle insertion," in *Proc. Haptics: Sci. Technol., Appl.*, 2022, vol. 13235, pp. 301–309.

[16] A. Barthel et al., "Haptic interface for robot-assisted ophthalmic surgery," in *Proc. IEEE 37th Annu. Int. Conf. Eng. Med. Biol. Soc.*, 2015, pp. 4906–4909.

[17] S. Yang, L. A. Lobes Jr, J. N. Martel, and C. N. Riviere, "Handheld-automated microsurgical instrumentation for intraocular laser surgery," *Lasers Surg. Med.*, vol. 47, no. 8, pp. 658–668, 2015.

[18] S. Yang, R. A. MacLachlan, J. N. Martel, L. A. Lobes, and C. N. Riviere, "Comparative evaluation of handheld robot-aided intraocular laser surgery," *IEEE Trans. Robot.*, vol. 32, no. 1, pp. 246–251, Feb. 2016.

[19] S. Yang, J. N. Martel, L. A. LobesJr, and C. N. Riviere, "Techniques for robot-aided intraocular surgery using monocular vision," *Int. J. Robot. Res.*, vol. 37, no. 8, pp. 931–952, 2018.

[20] S. L. Charreyron, E. Gabbi, Q. Boehler, M. Becker, and B. J. Nelson, "A magnetically steered endolaser probe for automated panretinal photocoagulation," *IEEE Robot. Automat. Lett.*, vol. 4, no. 2, pp. 17–23, Apr. 2019.

[21] R. Peter, S. Moreira, E. Tagliabue, M. Hillenbrand, R. G. Nunes, and F. Mathis-Ullrich, "Stereo reconstruction from microscopic images for computer-assisted ophthalmic surgery," *Int. J. Comput.- Assist. Radiol. Surg.*, vol. 20, no. 3, pp. 605–612, 2025.

[22] N. Piccinelli et al., "GEYEDANCE: An OCT-enhanced multi-modal feedback platform for robot-assisted ophthalmic surgery," *IEEE Trans. Med. Robot. Bionics*, vol. 7, no. 3, pp. 1017–1028, Aug. 2025.

[23] D. Gologorsky, R. Rosen, J. Giovinazzo, M. Jansen, G. Landa, and J. Lee, "Navigated retina laser therapy as a novel method for laser retinopexy of retinal tears," *Ophthalmic Surg., Lasers Imag. Retina*, vol. 49, no. 11, pp. 206–209, 2018.

[24] Y. M. Paulus et al., "Healing of retinal photocoagulation lesions," *Invest. Ophthalmol. Vis. Sci.*, vol. 49, no. 12, pp. 5540–5545, 2008.

[25] A. Jungo et al., "Unsupervised out-of-distribution detection for safer robotically guided retinal microsurgery," *Int. J. Comput. Assist. Radiol. Surg.*, vol. 18, no. 6, pp. 1085–1091, 2023.

[26] M. Briel et al., "Intraoperative adaptive eye model based on instrument-integrated OCT for robot-assisted vitreoretinal surgery," *Int. J. Comput.-Assist. Radiol. Surg.*, vol. 20, no. 5, pp. 881–889, 2025.

[27] M. Briel et al., "Intraoperative 3D reconstruction and geometric modeling using sensorized microsurgical instruments," *IEEE Trans. Med. Robot. Bionics*, vol. 7, no. 4, pp. 1479–1488, Nov. 2025.

[28] F.-Y. Lin, C. Bergeles, and G.-Z. Yang, "Biometry-based concentric tubes robot for vitreoretinal surgery," in *Proc IEEE. 37th Annu. Int. Conf. Eng. Med. Biol. Soc.*, 2015, pp. 5280–5284.